Control Engineering Practice 77 (2018) 138–149

Contents lists available at ScienceDirect

Control Engineering Practice

journal homepage: www.elsevier.com/locate/conengprac

Robust predictive control for heaving wave energy converters

Mohammed Jama[a], Addy Wahyudie[a,*], Hassan Noura[b]

[a] Electrical Engineering Department, United Arab Emirates University (UAEU), United Arab Emirates
[b] Aix-Marseille University, Marseille, France

ARTICLE INFO

Keywords:
Wave energy
Wave energy converter
Predictive control
Robust optimal control
Permanent magnet linear generator
Local model

ABSTRACT

In this paper, a novel robust model predictive controller (R-MPC) for wave energy converters (WECs) is proposed. The controller combines a constrained function-based predictive controller that is responsible for ensuring maximum power extraction and a local model that compensates for system parametric uncertainties and model mismatches. Laguerre polynomials have been deployed to alleviate the computational burden usually associated with the standard MPC techniques. The computer simulation results show that the R-MPC strategy has produced satisfactory and computationally efficient performance with respect to maximizing the captured power, increasing the power conversion efficiency, and enhancing the power take-off (PTO) utilization.

1. Introduction

Wave energy converters (WECs) are devices that capture the energy contained in traveling sea waves and convert them to useful energy (electricity) via a power take-off (PTO) system (Eriksson, 2007). A schematic of a grid-connected point absorber wave energy converter (WEC) is described in Fig. 1, which is made of a heaving body (buoy), a direct-drive permanent magnet linear generator (PMLG), an interconnecting tether, and auxiliary (restoring) springs. The energy capture capability of the WEC is dependent on the site of operation, buoy's geometry, PTO efficiency, and adopted control strategy.

Properly designed control strategy can increase the WEC energy yield, down size the required PTO rating, and prolong the lifetime of the system, thus making the system more feasible economically (Tedeschi & Molinas, 2012). Numerous WEC control techniques have been proposed in the literature, where almost all of them are based on the principle of reactive control proposed in Budal and Falnes (1980). Robust hierarchical control schemes, consisting of a high-level suboptimal buoy velocity reference generator and a low-level servo control loop, are presented in Fusco and Ringwood (2014a, b), Jama, Noura, Wahyudie, and Assi (2015) and Wahyudie, Jama, Saeed, Nandar, and Harib (2015, 2017).

Recently, the effectiveness of model predictive control (MPC) in controlling the WECs has been also discussed in the literature. Predictive controllers offer some exclusive features that have made them such an attractive control solution in the industry. To mention a few, predictive control, as the name implies, optimally generates the control law for each sampling instant based on the predicted future behavior of the system. In addition, it provides a ready platform to incorporate system limitations and constraints, which makes the anticipative nature of the controller further useful (Xi, Li, & Lin, 2013). However, these advantages come at the expense of increased computational complexity, especially for high order systems. In addition, the dependency of controllers on the system mathematical model jeopardizes its practical effectiveness. Therefore, having a fairly accurate mathematical model is of paramount importance (Xi et al., 2013). Classical constrained linear MPC strategies have been proposed to tackle the control problem in the mechanical side of the WEC (Hals, Falnes, & Moan, 2011; Li & Belmont, 2014). These efforts were based on maximizing captured energy of the WECs while limiting the buoy displacement and the PTO force. A modified linear MPC strategy, in which the PMLG copper losses are included, has been also addressed (Jaen, Andrade, & Santana, 2013). Furthermore, a constrained nonlinear MPC has been proposed to control two-body heaving WECs (Richter, Magana, Sawodny, & Brekken, 2013). In Li (2015), MPC method for controlling WECs using a combination of pseudo-spectral and differential flatness techniques is proposed. The method tackles the problems of non-convexity and non-linearity associated with the cost function, constraints, and the system model. A direct transcription optimal control law using Galerkin method along with a truncated Fourier series as basis functions is reported in Bacelli and Ringwood (2015).

In this work, a novel robust model predictive controller is proposed, which maximizes the energy output of the heaving WEC while respecting its physical limitations. The suggested control strategy is a genuine improvement over that proposed in Jama (2015) and Jama, Wahyudie,

* Corresponding author.
E-mail address: addy.w@uaeu.ac.ae (A. Wahyudie).

https://doi.org/10.1016/j.conengprac.2018.05.010
Received 8 May 2017; Received in revised form 10 May 2018; Accepted 22 May 2018
Available online 5 June 2018

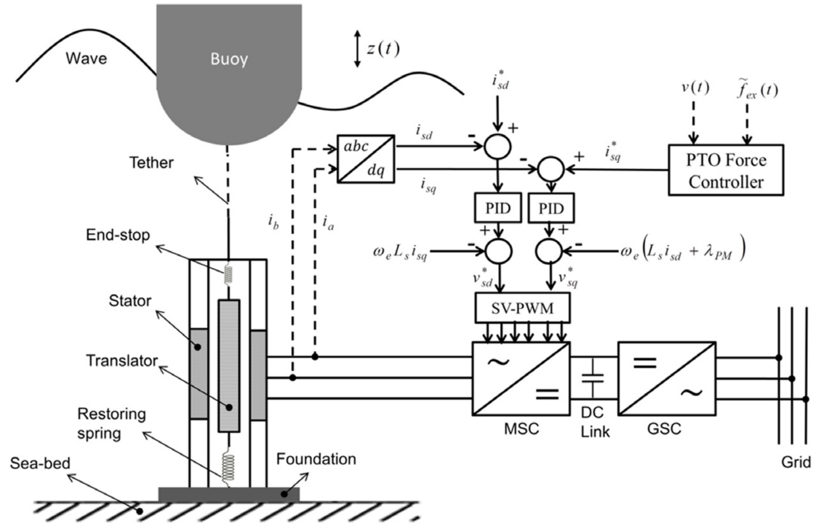

Fig. 1. Point absorber WEC system.

Assi, and Noura (2014). The controller consists of two main parts: (1) a sub-optimal reference-less function-based predictive controller and (2) a local model that compensates for the dynamics that are not captured by the predictive controller due to parametric uncertainties and external disturbances. The computational complexity usually associated with standard MPC is alleviated by parameterizing the PTO force using orthonormal polynomials. In addition, the local model ensures that the energy flow remains positive (i.e., from the sea to the grid) regardless of the sea-state characteristics. The local model contribution is designed so that it does not violate the limitations imposed by the predictive controller. The effectiveness of the proposed controller has been assessed through computer simulations by comparing it to other control strategies.

This paper is organized as follows. The point absorber WEC model is described in Section 2. The formulation of the proposed control strategy is presented in Section 3. The simulation results and the corresponding discussions are found in Section 4. Conclusions are given in Section 5.

2. Point absorber model

2.1. Equation of motion

The device is a single-body heaving wave energy converter oscillating against a fixed reference (i.e., the sea bed), as shown in Fig. 1. The submerged part of the buoy is semispherical. The forces acting on the system can be separated into two groups, the hydrodynamic forces $f_h(t)$ and the mechanical PTO forces $f_m(t)$ (Eriksson, 2007). Therefore, the governing equation of motion can be written as

$$f_h(t) + f_m(t) = ma(t), \tag{1}$$

where m is the total mass of the oscillating body and $a(t)$ is the buoy heave acceleration.

2.2. Hydrodynamic model

The hydrodynamic forces $f_h(t)$ can be decomposed into the following (Falnes, 2002):

$$f_h(t) = f_{ex}(t) + f_r(t) + f_b(t) + f_l(t), \tag{2}$$

where $f_{ex}(t)$ is the wave excitation force, $f_r(t)$ is the radiation force, $f_b(t)$ is the hydrostatic buoyancy force, and $f_l(t)$ is the losses force that could result from known or unknown hydrodynamic forces. Each of the mentioned forces can be modeled as

$$f_{ex}(t) = k_{ex}(t) * \eta(t) = \int_{-\infty}^{t} k_{ex}(\tau)\eta(t-\tau)d\tau, \tag{3a}$$

$$f_r(t) = -m_\infty a(t) - \int_0^t k_r(\tau)v(t-\tau)d\tau, \tag{3b}$$

$$f_b(t) = -S_b z(t), \tag{3c}$$

$$f_l(t) = -R_l v(t) - R_d\,|v(t) - v_w(t)|(v(t) - v_w(t)), \tag{3d}$$

where $k_{ex}(t)$ and $k_r(t)$ are the excitation and radiation convolution kernels, respectively. $\eta(t)$, $z(t)$ and $v(t)$ are the surface elevation of the incoming waves, the buoy heave displacement, and the buoy heave velocity, respectively. The coefficients S_b, R_l and R_d represent the buoyancy stiffness, hydrodynamic generic losses resistance and the viscous drag resistance, respectively. Note that $f_b(t)$ is a function of the buoy heave displacement $z(t)$, where $S_b = \rho g A_w$, that is A_w is the water plane area, ρ is the sea water density and g is the gravitational acceleration. The hydrodynamic losses force $f_l(t)$ is modeled as a summation of a linear and non-linear terms, in which the linear term represents a generic damping (resistive) force, whereas the nonlinear term models the viscous drag force according to Morison's equation (Ballard & Mann, 2013). The viscous drag force is modeled as quadratic function of the wave–buoy relative velocity, where $v_w(t)$ represents the water heave velocity when it is held undisturbed. The viscous drag resistance $R_d = 0.5\rho A_w C_d$, where C_d is the drag coefficient (McCormick, 2010). It is difficult to accurately determine C_d. However, the experimental results for a spherical buoy show that it typically varies between 0.7 and 1.5, depending on the Reynolds number (i.e., from 100 to 1×10^5) (Timmerman & Weelea, 1999). The constant m_∞ is the hydrodynamic added mass at infinite frequency.

Remark. It is important to mention here that due to the spherical geometry of the buoy, the buoy water plane area A_w varies as the buoy heaves, which will introduce non-linear dynamics to the hydrodynamic forces such as the excitation (Froude–Krylov) and hydro-static stiffness forces. However, if the maximum buoy stroke is kept noticeably lower than the buoy radius, the underlying non-linearities can be minimized.

The hydrodynamic software, WAMIT®, was used to solve the excitation and radiation problems (WAMIT, 2006). The frequency domain identification method proposed in Guo, Patton, Jin, and Lan (2018) was utilized to approximate the excitation convolution kernel with a causalized linear model, that is

$$\int_0^t k_{ex}(\tau)\eta(t-\tau)d\tau \approx \mathbf{C}_e\mathbf{q}_e(t)+\mathbf{D}_e\eta(t), \qquad \dot{\mathbf{q}}_e(t)=\mathbf{A}_e\mathbf{q}_e(t)+\mathbf{B}_e\eta(t), \tag{4}$$

where $\mathbf{q}_e(t) \in \mathbb{R}^{8\times1}$ is the excitation force approximation state vector, while the matrices $\mathbf{A}_e \in \mathbb{R}^{8\times8}$, $\mathbf{B}_e \in \mathbb{R}^{8\times1}$, and $\mathbf{C}_e \in \mathbb{R}^{1\times8}$ are the excitation state, input, and output matrices, respectively. Similarly, $k_r(t)$ is approximated by the 4th order linear model,

$$\int_0^t k_r(\tau)\eta(t-\tau)d\tau \approx \mathbf{C}_r\mathbf{q}_r(t), \qquad \dot{\mathbf{q}}_r(t)=\mathbf{A}_r\mathbf{q}_r(t)+\mathbf{B}_r v(t), \tag{5}$$

where $\mathbf{q}_r(t) \in \mathbb{R}^{4\times1}$ is the radiation kernel approximation state vector (Taghipoura, Pereza, & Moan, 2008).

2.3. Power take-off model

The mechanical forces $f_m(t)$ applied on the oscillating bodies (buoy and PMLG translator) are decomposed into

$$f_m(t)=f_u(t)+f_{rs}(t)+f_f(t), \tag{6}$$

where $f_u(t)$ is the controlled PTO force, $f_{rs}(t)$ is the restoring spring force, and $f_f(t)$ is the mechanical friction force. Each force is modeled as

$$f_u(t)=K_u i_{sq}(t), \tag{7a}$$
$$f_{rs}(t)=-S_{rs}z(t), \tag{7b}$$
$$f_f(t)=-R_c f_n sign(v(t))-R_v v(t). \tag{7c}$$

Note that $f_u(t)$ is manipulated by controlling the PMLG quadrature stator current $i_{sq}(t)$: this is performed by regulating the PMLG stator terminal voltage $v_s(t)$. The proportionality constant $K_u = 3\pi\lambda_{PM}/2p_w$, where λ_{PM} is the permanent magnet flux and p_w is the pole width of the PMLG (Boldea & Nasar, 1997; Feng, Zhang, Ju, & Sterling, 2008). To achieve maximum electromagnetic force per ampere, the direct current component i_{sd} is set to zero. The restoring force $f_{rs}(t)$ is modeled as a spring force, where S_{rs} is the spring coefficient (Eriksson, 2007). The friction force $f_f(t)$ is modeled nonlinearly as a combination of the Coulomb and viscous friction components, where λ_c and λ_v are the Coulomb and viscous friction coefficient, respectively, whereas f_n is the normal force between the parts in contact (Wang, Sun, Li, & Ye, 2001).

By using Park's transformation, the $d-q$ synchronous frame model of a surface-mounted PMLG is expressed as (Feng et al., 2008)

$$v_{sd}(t)=R_s i_{sd}(t)-\omega_e\lambda_{sq}(t)+\frac{d}{dt}(L_s i_{sd}(t)), \tag{8a}$$
$$v_{sq}(t)=R_s i_{sq}(t)+\omega_e\lambda_{sd}(t)+\frac{d}{dt}(L_s i_{sq}(t)), \tag{8b}$$
$$\lambda_{sd}(t)=L_s i_{sd}(t)+\lambda_{PM}, \tag{8c}$$
$$\lambda_{sq}(t)=L_s i_{sq}(t), \tag{8d}$$
$$\omega_e=\frac{\pi v(t)}{p_w}, \tag{8e}$$

where R_s, L_s, and ω_e are the stator resistance, inductance, and electrical angular frequency, respectively. λ_{sd} and λ_{sq} are the direct and quadrature stator flux linkages. The $d-q$ components of stator voltage, $v_{sd}(t)$ and $v_{sq}(t)$, are governed by the dc-link voltage, as shown in Fig. 1. Assuming that a space vector pulse width modulation (SV-PWM) technique is deployed, the maximum RMS stator current is formulated as follows (Sul, 2011)

$$I_s^{max}=\frac{1}{X_s}\sqrt{\left(\frac{m_a V_{dc}}{\sqrt{3}}\right)^2-\left(\omega_e^*\lambda_{PM}\right)^2}, \tag{9}$$

where m_a is the modulation index and V_{dc} is the dc-link voltage, and X_s is the synchronous reactance, defined as $X_s=\omega_e^* L_s$, where ω_e^* is the rated electrical angular frequency. The SV-PWM technique offers both high output voltage synthesis at the machine stator terminals while keeping the harmonic content reasonably low.

Table 1
Point absorber WEC model parameters.

Parameter (symbol)	Value	Unit
Buoy radius (r)	5	m
Buoy mass (m)	268×10^3	kg
Hydrodynamic infinite added mass (m_∞)	135×10^3	kg
Buoy water plane area (A_w)	78.54	m^2
Buoyancy stiffness coefficient (S_b)	789	kN/m
Restoring stiffness coefficient (S_{rs})	200	kN/m
Viscous drag coefficient (C_d)	1	–
Hydrodynamic losses resistance (R_l)	40	kN.s/m
Coulomb friction coefficient (λ_c)	50	kN
Viscous friction coefficient (λ_v)	20	kN
Rated machine force (F_u^{max})	1.5	MN
Rated translator stroke (z^{max})	3	m
Rated translator velocity (v^{max})	2	m/s
WEC oscillator natural frequency (ω_n)	1.57	rad/s
PMLG synchronous resistance (R_s)	0.29	Ω
PMLG synchronous inductance (L_s)	31	mH
Permanent magnet flux linkage (λ_{PM})	23	Wb
Pole width (p_w)	0.05	m
DC-link voltage (V_{dc})	3500	V
Modulation index (m_a)	1	–

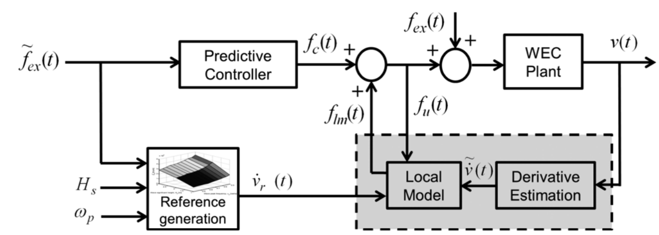

Fig. 2. Schematic of the proposed control strategy.

2.4. Linear state-space model

Substituting the nonlinear drag force by its linearized counterpart, $f_d(t) = R_d v(t)$ and setting $f_f(t) = 0$, the WEC continuous-time linear state space model is

$$\dot{\mathbf{x}}(t)=\mathbf{A}\mathbf{x}(t)+\mathbf{B}(f_u(t)+\tilde{f}_{ex}(t)), \qquad z(t)=\mathbf{C}_1\mathbf{x}(t), v(t)=\mathbf{C}_2\mathbf{x}(t), \tag{10}$$

where the state vector $\mathbf{x}(t) = [z(t)\ v(t)\ \mathbf{q}_r(t)^{\mathsf{T}}] \in \mathbb{R}^{6\times1}$ and the state matrices are

$$\mathbf{A}=\begin{bmatrix} 0 & 1 & \mathbf{0}_{1\times4} \\ \dfrac{-(S_b+S_{rs})}{m+m_\infty} & \dfrac{-R_l}{m+m_\infty} & \dfrac{-\mathbf{C_r}}{m+m_\infty} \\ \mathbf{0}_{4\times1} & \mathbf{B_r} & \mathbf{A_r} \end{bmatrix} \in \mathbb{R}^{6\times6}$$

$$\mathbf{B}=\begin{bmatrix} 0 \\ \dfrac{1}{m+m_\infty} \\ \mathbf{0}_{4\times1} \end{bmatrix} \in \mathbb{R}^{6\times1}, \mathbf{C}_1=\begin{bmatrix}1 & 0 & \mathbf{0}_{1\times4}\end{bmatrix} \in \mathbb{R}^{1\times6},$$

$$\mathbf{C}_2=\begin{bmatrix}0 & 1 & \mathbf{0}_{1\times4}\end{bmatrix} \in \mathbb{R}^{1\times6}.$$

Table 1 lists the system mechanical and electrical parameters. The wave excitation and radiation state matrices are included in Appendix A.

3. Control strategy design

As shown in Fig. 2, the control force produced by the PMLG, $f_u(t)$, consists of a predictive control component $f_c(t)$ and a local-model component $f_{lm}(t)$. The next section discusses how to compute these two force components.

3.1. Augmented model

The predictive controller is formulated based on the incremental control force $\Delta f_{c,k}$ instead of $f_{c,k}$, where the subscript k is the sample instant. The resultant augmented discrete state-space model is

$$\begin{aligned}\mathbf{w}_{k+1} &= \bar{\mathbf{A}}\mathbf{w}_k + \bar{\mathbf{B}}(\Delta f_{c,k} + \Delta\tilde{f}_{ex,k}),\\ z_k &= \bar{\mathbf{C}}_1\mathbf{w}_k, \upsilon_k = \bar{\mathbf{C}}_2\mathbf{w}_k,\end{aligned} \tag{11}$$

where $\mathbf{w}_k = [\Delta\mathbf{x}_k^{\mathsf{T}}\ z_k\ \upsilon_k]^{\mathsf{T}}$, and the augmented state matrices are defined as

$$\bar{\mathbf{A}} = \left[\begin{array}{c|cc} \mathbf{A}_d & 0 & 0\\ \mathbf{C}_{d1}\mathbf{A}_d & 1 & 0\\ \mathbf{C}_{d2}\mathbf{A}_d & 0 & 1\end{array}\right], \bar{\mathbf{B}} = \begin{bmatrix}\mathbf{B}_d\\ \mathbf{C}_{d1}\mathbf{B}_d\\ \mathbf{C}_{d2}\mathbf{B}_d\end{bmatrix},$$
$$\bar{\mathbf{C}}_1 = \left[\begin{array}{c|cc}\mathbf{0}_{1\times6} & 1 & 0\end{array}\right], \bar{\mathbf{C}}_2 = \left[\begin{array}{c|cc}\mathbf{0}_{1\times6} & 0 & 1\end{array}\right].$$

The subscript "d" denotes discrete, referring to the discrete formulation of the state matrices in (10). Note that in (10), $f_{ex}(t)$ is replaced with the estimated excitation force $\tilde{f}_{ex}(t)$ to distinguish between the actual excitation $f_{ex}(t)$ and its computed counterpart, $\tilde{f}_{ex}(t)$. Nevertheless, here we set $f_{ex}(t) \approx \tilde{f}_{ex}(t)$.

3.2. Predictive controller design

The incremental excitation force $\Delta\tilde{f}_{ex,k}$ is found by subtracting the previous excitation force sample from the current sample.

3.2.1. Predictive model

The predicted state trajectory is calculated sequentially over the prediction horizon N_p using (11), such as (Brekken, 2011)

$$\mathbf{W} = \mathbf{\Theta}_1\mathbf{w}_k + \mathbf{\Theta}_2(\Delta\mathbf{F}_c + \Delta\tilde{\mathbf{F}}_{ex}), \tag{12}$$

where

$$\mathbf{W} = \begin{bmatrix}\mathbf{w}_{k+1|k}\\ \mathbf{w}_{k+2|k}\\ \vdots\\ \mathbf{w}_{k+N_p|k}\end{bmatrix}, \Delta\mathbf{F}_c = \begin{bmatrix}\Delta f_{c,k|k}\\ \Delta f_{c,k+1|k}\\ \vdots\\ \Delta f_{c,k+N_c-1|k}\end{bmatrix}, \Delta\tilde{\mathbf{F}}_{ex} = \begin{bmatrix}\Delta\tilde{f}_{ex,k|k}\\ \Delta\tilde{f}_{ex,k+1|k}\\ \vdots\\ \Delta\tilde{f}_{ex,k+N_p-1|k}\end{bmatrix},$$
$$\mathbf{\Theta}_1 = \begin{bmatrix}\bar{\mathbf{A}}\\ \bar{\mathbf{A}}^2\\ \vdots\\ \bar{\mathbf{A}}^{N_p}\end{bmatrix}, \mathbf{\Theta}_2 = \begin{bmatrix}\bar{\mathbf{B}} & \mathbf{0} & \dots & \mathbf{0}\\ \bar{\mathbf{A}}\bar{\mathbf{B}} & \bar{\mathbf{B}} & \ddots & \mathbf{0}\\ \vdots & \ddots & \ddots & \vdots\\ \bar{\mathbf{A}}^{N_p-1}\bar{\mathbf{B}} & \bar{\mathbf{A}}^{N_p-2}\bar{\mathbf{B}} & \dots & \bar{\mathbf{B}}\end{bmatrix}.$$

The dimension of $\Delta\tilde{\mathbf{F}}_{ex}$ and $\Delta\mathbf{F}_c$ is N_c samples, where N_c represents the control horizon (where $N_c \le N_p$).

Remark. Here, $\Delta\tilde{\mathbf{F}}_{ex}$ future trajectory is estimated using (4), assuming that the wave elevation future trajectory is readily available. That could be achieved by prediction algorithms when it is implemented in real-time, such as Auto-Regressive (AR) models (Fusco & Ringwood, 2010). However, this is out of the scope of this work.

The predicted velocity trajectory $\mathbf{V}$ calculated over N_p samples is

$$\mathbf{V} = \mathbf{\Xi}_\upsilon\mathbf{w}_k + \mathbf{\Omega}_\upsilon(\Delta\mathbf{F}_c + \Delta\tilde{\mathbf{F}}_{ex}), \tag{13}$$

where

$$\mathbf{V} = \begin{bmatrix}\upsilon_{k+1|k}\\ \upsilon_{k+2|k}\\ \vdots\\ \upsilon_{k+N_p|k}\end{bmatrix}, \mathbf{\Xi}_\upsilon = \begin{bmatrix}\bar{\mathbf{C}}_2\bar{\mathbf{A}}\\ \bar{\mathbf{C}}_2\bar{\mathbf{A}}^2\\ \vdots\\ \bar{\mathbf{C}}_2\bar{\mathbf{A}}^{N_p}\end{bmatrix},$$
$$\mathbf{\Omega}_\upsilon = \begin{bmatrix}\bar{\mathbf{C}}_2\bar{\mathbf{B}} & \mathbf{0} & \dots & \mathbf{0}\\ \bar{\mathbf{C}}_2\bar{\mathbf{A}}\bar{\mathbf{B}} & \bar{\mathbf{C}}_2\bar{\mathbf{B}} & \ddots & \mathbf{0}\\ \vdots & \ddots & \ddots & \vdots\\ \bar{\mathbf{C}}_2\bar{\mathbf{A}}^{N_p-1}\bar{\mathbf{B}} & \bar{\mathbf{C}}_2\bar{\mathbf{A}}^{N_p-2}\bar{\mathbf{B}} & \dots & \bar{\mathbf{C}}_2\bar{\mathbf{B}}\end{bmatrix}.$$

3.2.2. Cost function

The controller cost function is based on maximizing the WEC captured energy E_{cap}. Therefore, the optimization problem is not formulated as a tracking control problem, which eliminates the need for a pre-calculated reference trajectory (Jama, Wahyudie, Assi, & Noura, 2013). Knowing that the instantaneous captured power P_{cap} at sampling instant k is calculated as the product of $f_{c,k}$ and υ_k, E_{cap} over an optimization window of length N_p and a sampling time T_s is found as (Hals et al., 2011)

$$\max\ E_{cap} = -T_s(\mathbf{V}^{\mathsf{T}}\mathbf{F}_c). \tag{14}$$

The objective of the predictive controller is to maximize E_{cap} or equivalently

$$\min\ E_{cap} = T_s(\mathbf{V}^{\mathsf{T}}\mathbf{F}_c). \tag{15}$$

Rewriting (15) in terms of $\Delta\mathbf{F}_c$, by sequentially solving $f_{c,k} = \Delta f_{c,k} + f_{c,k-1}$ over N_p samples, such that

$$\mathbf{F}_c = \mathbf{\Phi}f_{c,k-1} + \mathbf{P}\Delta\mathbf{F}_c, \tag{16}$$

where

$$\mathbf{\Phi} = \begin{bmatrix}1\\1\\ \vdots\\ 1\end{bmatrix} \in \mathbb{R}^{N_c\times1}, \mathbf{P} = \begin{bmatrix}1 & 0 & \dots & 0\\ 1 & 1 & \ddots & 0\\ \vdots & \ddots & \ddots & \vdots\\ 1 & 1 & \dots & 1\end{bmatrix} \in \mathbb{R}^{N_c\times N_c}.$$

By substituting (13) and (16) into (15), we get

$$\begin{aligned}E_{cap} = T_s[&\mathbf{w}_k^{\mathsf{T}}\mathbf{\Xi}_\upsilon^{\mathsf{T}}\mathbf{\Phi}f_{c,k-1} + \mathbf{w}_k^{\mathsf{T}}\mathbf{\Xi}_\upsilon^{\mathsf{T}}\mathbf{P}\Delta\mathbf{F}_c + \Delta\mathbf{F}_c^{\mathsf{T}}\mathbf{\Omega}_\upsilon^{\mathsf{T}}\mathbf{\Phi}f_{c,k-1}\\ &+ \Delta\tilde{\mathbf{F}}_{ex}^{\mathsf{T}}\mathbf{\Omega}_\upsilon^{\mathsf{T}}\mathbf{\Phi}f_{c,k-1} + \Delta\mathbf{F}_c^{\mathsf{T}}\mathbf{\Omega}_\upsilon^{\mathsf{T}}\mathbf{P}\Delta\mathbf{F}_c\\ &+ \Delta\mathbf{F}_{ex}^{\mathsf{T}}\mathbf{\Omega}_\upsilon^{\mathsf{T}}\mathbf{P}\Delta\mathbf{F}_c].\end{aligned} \tag{17}$$

Knowing that the initial control force $f_{c,k-1}$ is zero (operation starts from rest), the captured energy expression boils down to

$$E_{cap} = T_s[\mathbf{w}_k^{\mathsf{T}}\mathbf{\Xi}_\upsilon^{\mathsf{T}}\mathbf{P}\Delta\mathbf{F}_c + \Delta\mathbf{F}_c^{\mathsf{T}}\mathbf{\Omega}_\upsilon^{\mathsf{T}}\mathbf{P}\Delta\mathbf{F}_c + \Delta\mathbf{F}_{ex}^{\mathsf{T}}\mathbf{\Omega}_\upsilon^{\mathsf{T}}\mathbf{P}\Delta\mathbf{F}_c]. \tag{18}$$

The control force trajectory $\Delta\mathbf{F}_c$ is approximated by a finite number of Laguerre polynomials, which are orthonormal complete basis functions (Wang, 2001; Yousef & Kassem, 2012). The Laguerre polynomials written in the compact state space form can be expressed as (Wang, 2001)

$$\mathbf{L}_{k+1} = \mathbf{A}_\ell\mathbf{L}_k, \tag{19}$$

where

$$L_k = [\ell_{1,k}\ \ell_{2,k}\ \dots\ \ell_{N,k}]^{\mathsf{T}},$$
$$\mathbf{A}_\ell = \begin{bmatrix}\beta & 0 & \dots & \dots & 0\\ \gamma & \beta & \ddots & \ddots & 0\\ -\beta\gamma & \gamma & \ddots & \ddots & \vdots\\ \vdots & \vdots & \ddots & \ddots & \vdots\\ (-\beta)^{N-2}\gamma & (-\beta)^{N-3}\gamma & \dots & \gamma & \beta\end{bmatrix} \in \mathbb{R}^{N\times N},$$

where ℓ_k is the discrete-time Laguerre polynomial at time instant k, $\mathbf{A}_\ell$ is the state matrix of the Laguerre model, and $\gamma = (1-\beta^2)$, where β is the pole of the Laguerre polynomials and N is the total number of these polynomials. At every sampling instant k, $\Delta f_{c,k}$ can be approximated as a weighted sum of Laguerre polynomials

$$\Delta f_{c,k} \approx \sum_{j=0}^{N} c_j\ell_{j,k}, \tag{20}$$

where $c_1, c_2, \dots, c_N$ represent the Laguerre coefficients. Similarly, this is extended to approximate the entire control trajectory over N_c, such as

$$\Delta\mathbf{F}_c = \mathbf{L}^{\mathsf{T}}\boldsymbol{\sigma}, \tag{21}$$

where

$$\mathbf{L} = \left[L_k \; L_{k+1} \; \dots \; L_{k+N_c-1}\right]^{\mathsf{T}},$$

$$\boldsymbol{\sigma} = \left[c_1 \; c_2 \; \dots \; c_N\right]^{\mathsf{T}}.$$

Here, $\mathbf{L}$ is computed once for every N and β. A good practice to determine N is to approximate the impulse response of the system (Wang, 2001). As shown in Fig. 3, the impulse response of the model presented in (10) is well approximated up to 10 s using 15 Laguerre polynomials, where their poles are placed at $\beta = 0.8$. Substituting (21) into the cost function depicted in (18), we get

$$E_{cap} = \boldsymbol{\sigma}^{\mathsf{T}}\boldsymbol{\Upsilon}\boldsymbol{\sigma} + 2\boldsymbol{\sigma}^{\mathsf{T}}\mathbf{H}, \tag{22}$$

where

$$\boldsymbol{\Upsilon} = T_s\mathbf{L}\boldsymbol{\Omega}_v\mathbf{P}\mathbf{L}^{\mathsf{T}},$$

$$\mathbf{H} = 0.5T_s\mathbf{L}[\mathbf{P}^{\mathsf{T}}\boldsymbol{\Xi}_v\mathbf{w}_k + \mathbf{P}^{\mathsf{T}}\boldsymbol{\Omega}_v\Delta\tilde{\mathbf{F}}_{ex}].$$

The quadratic programming (QP) problem depicted in (22) is convex because the symmetric matrix $(\boldsymbol{\Upsilon} + \boldsymbol{\Upsilon}^{\mathsf{T}})/2$ is positive definite in $\mathfrak{R}^n$. The convexity property will ensure that any local solution for the QP problem is also an optimum solution (Yang, 2010).

Remark. As illustrated, the selection of β and N depends on the dynamics of the WEC oscillator, which can be characterized by the system intrinsic damping and natural frequency. Therefore, the selection of β and N is independent of the sea-state environment (wave height and frequency), which in turn will make the controller tuning process much easier (i.e., no need for sea waves spectral inspection).

3.2.3. Constraints formulation

The cost function in (22) is optimized subject to linear inequality constraints to address the possible system limitations. The limitations on the PTO control force are imposed as

$$-\mathbf{F}_c^{max} \le \mathbf{F}_c \le \mathbf{F}_c^{max}, \tag{23}$$

where the vector $\mathbf{F}_c^{max} = [f_c^{max} \; f_c^{max} \; \dots \; f_c^{max}] \in \mathbb{R}^{N_c \times 1}$ represents the maximum bi-directional limitation of the PTO force. Substituting (16) and (21) into (23), we get

$$-\mathbf{F}_c^{max} \le \boldsymbol{\Phi} f_{c,k-1} + \mathbf{P}\mathbf{L}^{\mathsf{T}}\boldsymbol{\sigma} \le \mathbf{F}_c^{max}. \tag{24}$$

Constraints on the predicted buoy heave displacement trajectory are imposed to confine the buoy displacement to the system's maximum stroke that is

$$-\mathbf{Z}^{max} \le \mathbf{Z} \le \mathbf{Z}^{max}, \tag{25}$$

where $\mathbf{Z}^{max} = [z^{max} \; z^{max} \; \dots \; z^{max}] \in \mathbb{R}^{N_p \times 1}$ and similar to (13), $\mathbf{Z}$ is described as

$$\mathbf{Z} = \boldsymbol{\Xi}_z\mathbf{w}_k + \boldsymbol{\Omega}_z(\mathbf{L}^{\mathsf{T}}\boldsymbol{\sigma} + \Delta\tilde{\mathbf{F}}_{ex}). \tag{26}$$

The matrices $\boldsymbol{\Xi}_z$ and $\boldsymbol{\Omega}_z$ are formulated similar to $\boldsymbol{\Xi}_v$ and $\boldsymbol{\Omega}_v$, respectively, except that $\bar{\mathbf{C}}_2$ is replaced with $\bar{\mathbf{C}}_1$. Likewise, constraints are imposed on the buoy velocity using (13), such that

$$-\mathbf{V}^{max} \le \boldsymbol{\Xi}\mathbf{w}_k + \boldsymbol{\Omega}(\mathbf{L}^{\mathsf{T}}\boldsymbol{\sigma} + \Delta\tilde{\mathbf{F}}_{ex}) \le \mathbf{V}^{max}. \tag{27}$$

The set of linear inequality constraints shown in (24), (26), and (27) along with the cost function in (22) form a convex constrained QP problem.

Remark. Note that the QP problem is reduced to the problem of optimizing a finite set of coefficients $\boldsymbol{\sigma} \in \mathbb{R}^{N \times 1}$, instead of optimizing $\Delta\mathbf{F}_c \in \mathbb{R}^{N_c \times 1}$. Fortunately, the system dynamics can be well modeled by a small number of Laguerre coefficients (i.e., $N \ll N_c$), which significantly alleviates the computational complexity of the problem. Using Laguerre polynomials also reduces the size of the constraints inequality. Therefore, using function-based predictive control permits prolonging the prediction horizon, without significantly increasing the problem dimensionality, which facilitates the real-time implementation of the strategy (Yousef & Kassem, 2012).

3.3. Ultra-local model formulation

In an attempt to address the model imperfections, the computed control force $f_{c,k}$ has to be corrected. Furthermore, the reactive nature of the predictive controller in aiming to minimize the power returned to the sea might cause the time-averaged electrical power to be reversed (i.e., the PMLG might work as a motor).

An ultra-local model (ULM) can be used to overcome the aforementioned challenges. This model stems from the famous implicit function theorem, in which a single-input single-output dynamic system can be expressed by a continuous implicit function of the form (Fliess & Join, 2008)

$$\boldsymbol{\chi}(t, y, \dot{y}, \dots, y^{(n)}, u, \dot{u}, \dots, u^{(m)}) = 0, \tag{28}$$

where y and u denote the system output and input, respectively, whereas n and m are positive integers representing the highest derivative order for the output and input, respectively.

Definition 1. Assume that χ is a continuous function with continuous partial derivatives defined on an open set $\mathbb{S}$. If $\frac{\partial \chi}{\partial y^{(i)}} \not\equiv 0$ at a point P, where $P \in \mathbb{S}$, there exists a neighboring region $\mathfrak{R}$ about P such that for any point

$$(t, y, \dot{y}, \dots, y^{(i-1)}, y^{(i+1)}, \dots, y^{(n)}, u, \dot{u}, \dots, u^{(m)}) \in \mathfrak{R}$$

there is a unique y^i such that (29) holds and thus

$$y^{(i)} = \Pi(t, y, \dot{y}, \dots, y^{(i-1)}, y^{(i+1)}, \dots, y^{(n)}, u, \dot{u}, \dots, u^{(m)})$$

over $\mathfrak{R}$ (Krantz, 2002).

Obviously, Π is an unknown function. However, it can be approximated by a local model that is only valid for a short time (hence the name *ultra-local model*), which is formulated as (Fliess & Join, 2013)

$$y_k^{(i)} = \Gamma_{k-1} + \alpha u_k, \tag{29}$$

where $y_k^{(i)}$ is the ith order derivative of the output, which is the buoy heave velocity v_k, Γ_{k-1} is a function estimated online to capture system dynamics, u_k is the input variable, that is the PTO force $f_{c,k}$, and α is a weighting factor tuned by the practitioner depending on the system under investigation. Note that i is usually set to 1 or 2 based on the system's model order. Therefore, referring to the system at our disposal, which is a 2nd order system, setting $i = 1$ is sufficient (Fliess & Join, 2013). By re-arranging (29) and writing it in terms of the WEC variables, we get

$$f_{lm,k} = \frac{1}{\alpha}(\dot{v}_{r,k} - \Gamma_{k-1}), \tag{30}$$

where $f_u(k)$ represents the overall PTO force (i.e., including $f_c(k)$). Note that $\dot{v}_{r,k}$ is the 1st derivative of the buoy reference buoy velocity. Similarly, the one sample delayed unknown function Γ_{k-1} is estimated as

$$\Gamma_{k-1} = \tilde{\dot{v}}_{k-1} - \alpha f_{lm,k-1}, \tag{31}$$

where $\tilde{\dot{v}}_{k-1}$ is the $(k-1)$th sample 1st derivative of the measured buoy velocity, whereas $f_{lm,k-1}$ is the $(k-1)$th sample of the local model force. By substituting (31) into (30), the $f_{lm,k}$ becomes

$$f_{lm,k} = f_{lm,k-1} + \frac{1}{\alpha}(\dot{v}_{r,k} - \tilde{\dot{v}}_{k-1}). \tag{32}$$

The overall PTO force $f_{u,k}$ is the algebraic summation of $f_{lm,k}$ and $f_{c,k}$, as shown in Fig. 2. This control scheme is referred to as a *robust* model predictive controller (R-MPC).

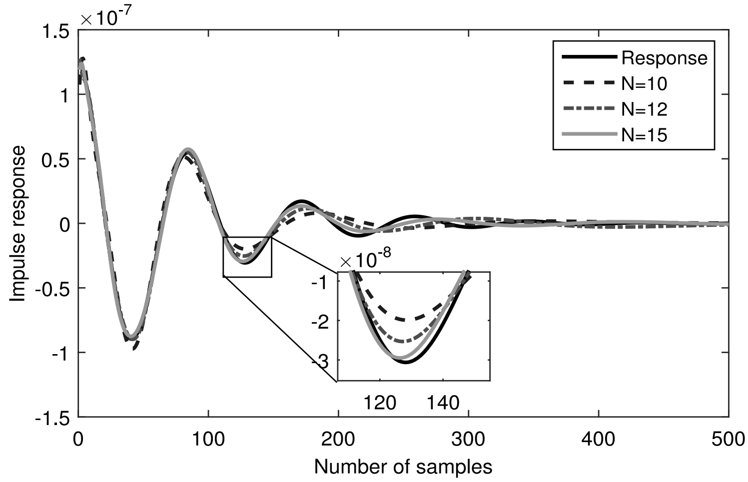

Fig. 3. Impulse response approximation using Laguerre polynomials for sampling time $T_s = 0.1$ s.

To ensure that $f_{lm,k}$ abides by the system constraints, the ULM weighting factor α is expressed in such a way that it works like an adaptive weighting factor,

$$\alpha = \gamma_0 \left(1 - \gamma_1 \mathbb{H}\left(|f_{u,k-1}| - F_u^{max}\right)\right), \tag{33}$$

where γ_0 is a constant selected by the designer, and γ_1 is a weighting factor ($0 \le \gamma_1 \le 1$) responsible for reducing the contribution of f_{lm} before violating the PTO force limitation. The function $\mathbb{H}$ is the Heaviside function that switches on or off the f_{lm} limiting function, using the previously measured or estimated overall PTO force $f_{u,k-1}$ and the PTO force constraint F_u^{max}.

Remark. The computation of $f_{lm,k}$ requires the estimation of $\dot{v}_{k-1}$. Ideal differentiation of the measured signal should be avoided since it might be contaminated with significant noise. Therefore the method proposed in Reger, Ramirez, and Fliess (2005) has been utilized.

3.4. Reference velocity calculation

Note that the local model needs a reference velocity $v_{r,k}$ as depicted in (32). A constrained optimization problem is constructed with an objective of maximizing the absorbed energy E_{abs} across a short finite window N_w (Falnes, 2002; Hals et al., 2011). Therefore, the reference velocity $v_{r,k}$ at sampling instant k is computed by minimizing the following cost function

$$\begin{aligned} v_{r,k}^* &= \arg\min T_s \sum_{k=1}^{N_w} \left(P_{r,k} + P_{l,k} - P_{ex,k}\right), \\ &\text{subject to } \ |z_k| \le z^{max}, \end{aligned} \tag{34}$$

where $P_{ex,k}$, $P_{r,k}$ and $P_{l,k}$ are the excitation, radiation, and the hydrodynamic losses powers, respectively. After discretizing the variables and state matrices shown in (10), $P_{ex,k} = \tilde{f}_{ex,k} v_k$, $P_{r,k} = \mathbf{C}_r \mathbf{q}_{r,k} v_k$, and $P_{l,k} = R_l v_k$. By solving (34) N_w samples forward into the future, the quadratic programming problem can be expressed in vector form, where the reference velocity trajectory $\mathbf{V}_{r,k} \in \mathbb{R}^{N_w \times 1}$ at sampling instant k can be computed as follows:

$$\begin{aligned} \mathbf{V}_{r,k}^* &= \arg\min T_s \left[\mathbf{V}_{r,k}^{\mathsf{T}} \mathbf{Q}_v \mathbf{V}_{r,k} + \left(\mathbf{Q}_x \mathbf{x}_k - \mathbf{R}_l - \tilde{\mathbf{F}}_{ex,k}\right)^{\mathsf{T}} \mathbf{V}_{r,k}\right], \\ &\text{subject to } \ \mathbf{Q}_z \mathbf{V}_{r,k} \le \mathbf{H}, \end{aligned} \tag{35}$$

Here, $\mathbf{x}_k$ is the discrete counterpart of the space vector in (10), whereas $\tilde{\mathbf{F}}_{ex,k}$ is the estimated N_w- samples length excitation force trajectory. More details about the objective function shown in (35) are presented in Appendix B. To ease the computational burden associated with solving (35) at every sampling instant, the optimization has been carried out off-line for various waves with different significant heights H_s and peak frequencies ω_p and a look-up table containing the optimum average hydrodynamic resistance $\bar{R}^*(H_s, \omega_p)$ has been built. A few important points should be highlighted here:

1. Since $v_k^* = 0$ at $z_k = z^{max}$, due to $R^* \Rightarrow \infty$, the time-averaged reciprocal resistance $1/\bar{R}^*$, which is equal to $\mathbf{V}_{r,k}^*/\tilde{\mathbf{F}}_{ex,k}$ is calculated.
2. The look-up table is accessed through H_s and ω_p by performing spectral analysis of the real-time wave measurements (typically every 20–30 min).
3. The reference velocity at the sampling instant k is then computed on-line as $v_{r,k} = \tilde{f}_{ex,k}/\bar{R}^*$.

The local model contribution can be simplified by tuning $\bar{R}_{opt}$ at specific (H_s, ω_p). This is referred to as the simplified robust model predictive controller (SR-MPC).

3.5. Stability analysis

In this section, the stability of the proposed control strategy is studied. The system under investigation is stable as an open loop system with a settling time of the order of a few seconds. However, since the control problem is formulated as a constrained MPC problem, it has to be handled as a nonlinear control problem, especially when the constraints become active.

Lemma. *The closed loop asymptotic stability of the* MPC *system can be achieved given the assumptions, a terminal state equality constraint is used, that is* $\mathbf{w}_{k+N_p} = \mathbf{0}$, *and there exists an optimal solution* $\boldsymbol{\sigma}^*$ *of the cost function* E_{cap}, *subject to the inequality constraints and the terminal state constraint* (Wang, 2009).

Proof. The cost function in (18) is based on the system's captured energy, which is positive definite. Therefore, it is a valid Lyapunov candidate function. Set the optimal cost function at time instant k as a Lyapunov function,

$$\mathscr{L}_k^* = \Delta\mathbf{F}_{c,k}^{\mathsf{T}} \boldsymbol{\Omega}_v^{\mathsf{T}} \mathbf{P} \Delta\mathbf{F}_{c,k} + \Delta\mathbf{F}_{c,k} [\mathbf{w}_k^{\mathsf{T}} \boldsymbol{\Xi}_v^{\mathsf{T}} \mathbf{P} + \Delta\mathbf{F}_{ex,k}^{\mathsf{T}} \boldsymbol{\Omega}_v^{\mathsf{T}} \mathbf{P}],$$

where $\Delta\mathbf{F}_{c,k} = \mathbf{L}^{\mathsf{T}} \boldsymbol{\sigma}^* = [\Delta f_{c,k}, \Delta f_{c,k+1}, \dots, \Delta f_{c,k+N_p-1}]$. Similarly, the Lyapunov function at time instant $k+1$ is

$$\mathscr{L}_{k+1}^* = \Delta\mathbf{F}_{c,k+1}^{\mathsf{T}} \boldsymbol{\Omega}_v^{\mathsf{T}} \mathbf{P} \Delta\mathbf{F}_{c,k+1} + \Delta\mathbf{F}_{c,k+1} [\mathbf{w}_{k+1}^{\mathsf{T}} \boldsymbol{\Xi}_v^{\mathsf{T}} \mathbf{P} + \Delta\mathbf{F}_{ex,k+1}^{\mathsf{T}} \boldsymbol{\Omega}_v^{\mathsf{T}} \mathbf{P}].$$

In order to satisfy the terminal state constraint $\mathbf{w}_{k+N_p} = \mathbf{0}$, a feasible solution (i.e., sub-optimal) is sought. The feasible Lyapunov function

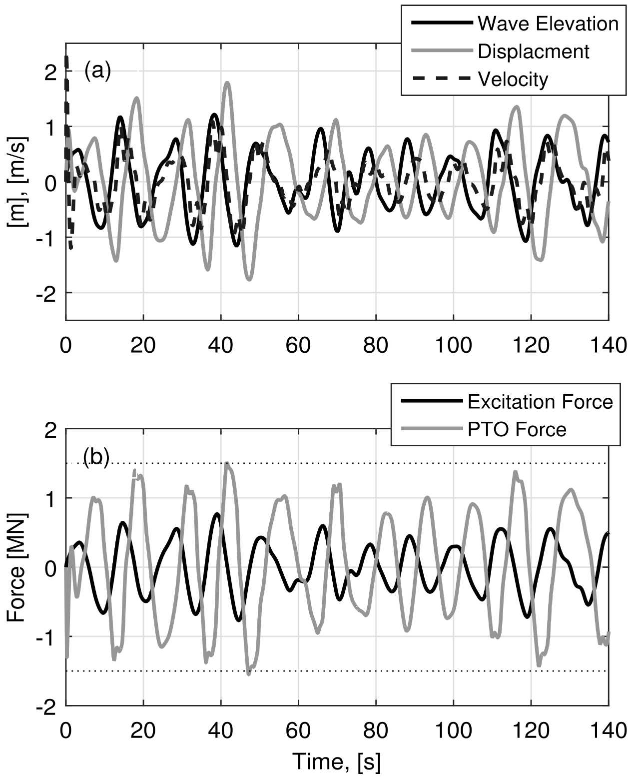

Fig. 4. WEC mechanical dynamics under R-MPC when an irregular sea state of $H_s = 2$ m and $\omega_p = 0.5$ rad/s is applied (a) wave elevation and buoy heave displacement and velocity (b) wave excitation force and the controlled PTO force.

$\mathscr{L}_{k+1}$ at time instant $k+1$ is similar to $\mathscr{L}^*_{k+1}$, except that the optimal control sequence is replaced with a feasible control sequence

$\mathbf{\Delta F}_{c,k+1} = [\Delta f_{c,k+1}, \Delta f_{c,k+2}, \ldots, \Delta f_{c,k+N_p-1}, 0]$.

Taking the difference between $\mathscr{L}_{k+1}$ and $\mathscr{L}^*_k$ and , we get

$$\mathscr{L}_{k+1} - \mathscr{L}^*_k = -\frac{2\Delta f_{c,k}\Delta f_{c,k}}{m+m_\infty} + \Delta f_{c,k}(v_k + a_k), \tag{36}$$

where v_k and a_k is the system velocity and acceleration at time instant k, respectively. Note that

$$\left|\frac{2\Delta f_{c,k}\Delta f_{c,k}}{m+m_\infty}\right| > \left|\Delta f_{c,k}(v_k + a_k)\right|.$$

Therefore, $\mathscr{L}_{k+1} - \mathscr{L}^*_k \leq 0$, and knowing that $\mathscr{L}^*_{k+1} \leq \mathscr{L}_{k+1}$, then $\mathscr{L}^*_{k+1} - \mathscr{L}^*_k \leq 0$, implying negative definiteness.

Remark. The local model contribution $f_{lm,k}$ is a fraction of the force produced by the MPC loop. Moreover, the weighting factor expressed in (33) ensures that the overall control force $f_{u,k}$ stays within the control limitations introduced by the MPC. Therefore, the system stability is maintained.

4. Results and discussions

The proposed controller was assessed by carrying out simulations using MATLAB/Simulink. The system was excited by regular and irregular sea-states. JONSWAP spectrum was utilized to generate irregular sea-states (McCormick, 2010). The performance of the developed robust model predictive controller (R-MPC) is compared to the base predictive controller (B-MPC) (i.e., $f_{lm}(k) = 0$), the simplified robust model predictive controller (SR-MPC), latching control (LC) strategy and the resistive loading (RL) strategy. The latching control (LC) is a strategy in which the buoy velocity is forced to become in phase with the wave excitation force (phase control) by latching it at $v(t) = 0$ and unlatching it at $f_{ex}(t) = 0$. The latching method used in this work does not require any prediction, hence its a sub-optimal strategy (Sheng, Alcorn, & Lewis, 2015). Another sub-optimal method used in this work is RL strategy. Despite its simplicity and low cost, a well-tuned RL strategy can be fairly effective (Jaen et al., 2013). More details on both LC and RL strategies are provided in Appendix C. In this work, $\bar{R}_{opt}$ used to generate $v_r(k)$ for SR-MPC and the coefficients of the RL strategy are tuned at $\omega_p = 0.7$ rad/s and $H_s = 2$ m. To assess the effectiveness of the different controllers, the average mechanical captured power $\bar{P}_{cap}$, the average electrical converted power $\bar{P}_{conv}$, and the wave-to-wire efficiency, $\bar{P}_{conv}/\bar{P}_w$, are recorded. Here $\bar{P}_w$ is the average wave power. To check the reactive power content, the peak-to-average converted power ratio, $\hat{P}_{conv}/\bar{P}_{conv}$, where $\hat{P}_{conv}$ is the peak converted power, is computed. Practically, the WEC design used in this study is over-sized. However, that does not prevent the fact that the proposed method can be easily used to control WEC systems with smaller ratings or even different topologies.

4.1. Nominal operation

The dynamics of the WEC under R-MPC strategy and in the presence of an irregular wave of $H_s = 2$ m and $\omega_p = 0.5$ rad/s are shown in Figs. 4–6. As shown in Fig. 4, the buoy velocity has almost the same harmonic structure as the wave excitation force while being almost in phase (resonance). The buoy displacement and velocity are well within the system constraints. In addition, $f_u(t)$ is constrained within its predefined limits (±1.5 MN). The PMLG $i_{sq}(t)$ is regulated as per the reference signal $i^*_{sq}(t)$, as shown in Fig. 5(a). Note that $i_{sq}(t)$ reaches its maximum (approximately ±700 A) at instants when $f_u(t)$ approaches ±1.5 MN.

The instantaneous captured and converted powers along with their time-averaged values under the R-MPC strategy are shown in Fig. 6(a). The WEC under the R-MPC has managed to capture $\bar{P}_{cap} = 0.107$ MW and convert $\bar{P}_{conv} = 0.032$ MW. Therefore the resultant PTO conversion efficiency $\bar{P}_{conv}/\bar{P}_{cap} = 30\%$. The corresponding wave-to-wire conversion efficiency is $\bar{P}_{conv}/\bar{P}_w = 12.22\%$. The mechanical side of the WEC (i.e., the water–buoy interaction) shows bidirectional power flow due to the presence of reactive power. However, the average real power captured by the buoy is still positive (from wave to the buoy), where the ratio of the peak-to-average captured power $\hat{P}_{cap}/\bar{P}_{cap} = 7.83$, indicating low reactive power content. The PMLG suffers from a high reactive power content, which is indicated by the ratio of the peak-to-average converted power $\hat{P}_{conv}/\bar{P}_{conv} = 16.26$.

Although issuing more PTO force (as shown in Fig. 6(b)), the unconstrained B-MPC failed to capture enough power. Instead, the captured power is dominated by large reactive power content. The PMLG under R-MPC produced less control effort than when the constrained B-MPC strategy is in charge, as depicted in Fig. 6(b). The accumulated captured energy is calculated under the R-MPC and compared to the B-MPC and RL strategies. As shown in Fig. 6(c), the R-MPC outperformed its rivals ($E_{cap} = 4.18$ kWh). Although monotonically increasing, both R-MPC and the constrained B-MPC ($E_{cap} = 2.10$ kWh) suffer from ripples, indicating energy reversals, unlike the RL strategy ($E_{cap} = 1.57$ kWh), where the unidirectional energy nature makes the energy curve smooth. The unconstrained B-MPC strategy produced the poorest performance ($E_{cap} = 0.47$ kWh).

4.2. Effect of wave characteristics on the WEC performance

Regular waves of various heights and frequencies are applied and the performance of the WEC under different control strategies is examined. First, for a significant wave height of $H_s = 2$ m, the effect of varying the wave frequency on the WEC performance is shown in Fig. 7. Obviously,

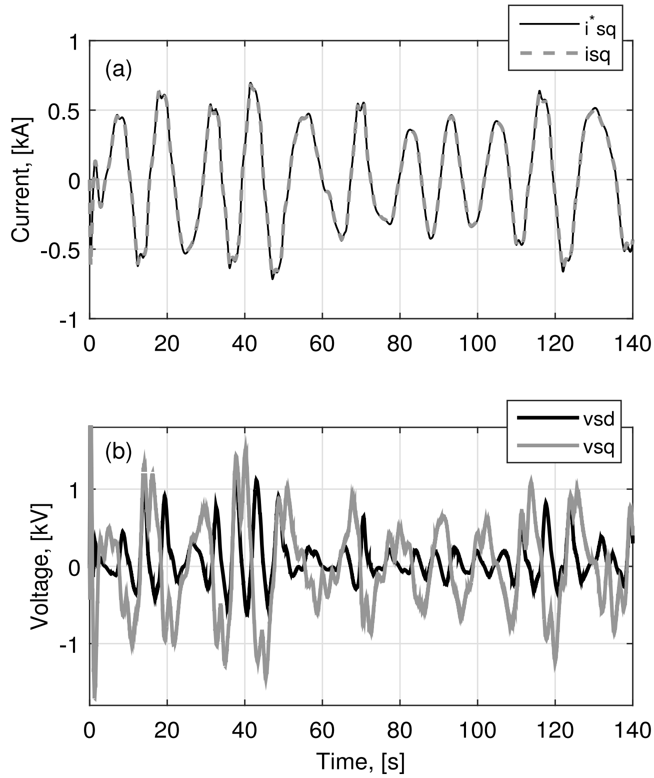

Fig. 5. WEC electrical dynamics under R-MPC when an irregular sea state of $H_s = 2$ m and $\omega_p = 0.5$ rad/s is applied (a) the reference and actual quadrature stator currents (b) the $d-q$ stator voltage components.

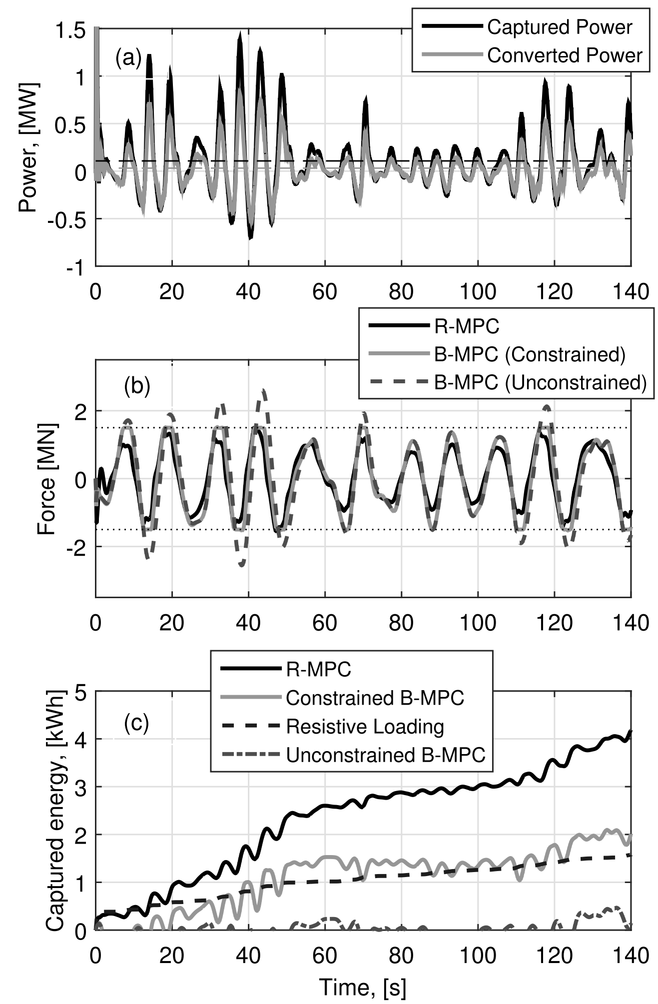

Fig. 6. WEC dynamics when an irregular sea state of $H_s = 2$ m and $\omega_p = 0.5$ rad/s is applied (a) Instantaneous captured and converted powers along with their time-averaged values under R-MPC (b) PTO control force under different control strategies (c) The accumulated captured energy under different control strategies.

under R-MPC, SR-MPC, LC and RL, the average converted power flow remains positive (i.e., from the sea to the grid) across a range of wave frequencies, whereas under B-MPC the system fails to maintain unidirectional power flow, especially for $\omega_p > 0.75$ rad/s. Although the system under the B-MPC strategy uses more PTO resources, the power converted is greater for R-MPC, SR-MPC, LC and RL. Large reactive power content is recorded under the B-MPC strategy, as shown in Fig. 7(d). As expected, the RL strategy produces the highest conversion efficiency (around 60%), whereas the conversion efficiency under R-MPC increases as ω_p increases, until it nearly approaches that of the RL strategy, as shown in Fig. 7(b). The LC strategy produced poor performances at $\omega_p < 0.7$ rad/s, with converted power values less than those produced by the RL strategy. However, the performance significantly improved at higher ω_p values. Note that the SR-MPC produces a performance close to that produced by the R-MPC at low wave frequencies (i.e., ≤ 0.7 rad/s). However, the performance deteriorates as ω_p approaches 1 rad/s. Using more PTO force at $\omega_p > 0.7$ rad/s does not seem to make the SR-MPC yield more energy compared to R-MPC, as shown in Fig. 7(c). The peak-to-average ratio of the converted power for the R-MPC is low, almost comparable to that of the RL (less than 5), which indicates low reactive power content, resulting in an increase in the useful real power (see Fig. 7(d)).

Similarly, for a fixed peak wave frequency $\omega_p = 0.55$ rad/s, H_s is varied (from 1 to 3 m) and the performance of the WEC is recorded for the different controllers. As shown in Fig. 8(a), $\bar{P}_{conv}$ monotonically increases for the R-MPC and RL controllers, with the R-MPC being superior to the other controllers. Remarkably, the performance of SR-MPC is very close to that of the R-MPC in $\bar{P}_{conv}$ up to $\omega_p = 0.7$ rad/s, at which the SR-MPC is tuned. This is also obvious in the conversion efficiency, where it peaks at $\omega_p = 0.7$ rad/s to be equal to that produced by the R-MPC, as shown in Fig. 8(b). For $H_s < 2$ m, the $\bar{P}_{conv}$ for the B-MPC is negative (i.e., the PMLG is operating as a motor). The $\hat{P}_{conv}/\bar{P}_{conv}$ remains below 10 for the R-MPC and the RL, as shown in Fig. 8(d).

4.3. Sensitivity to parametric uncertainty and un-modeled dynamics

The robustness of the developed R-MPC is examined by applying structured uncertainties, i.e., varying the model parameters in the plant. Another robustness test is carried out by incorporating un-modeled dynamics through adding a nonlinear viscous drag force to the plant model. In (10), the hydrostatic stiffness coefficient S_b is held constant, since A_w is assumed fixed. However, for the submerged hemispherical buoy, A_w might vary as the buoy oscillates. Another potential source of parametric uncertainty is the hydrodynamic losses resistance coefficient R_l, due to the ambiguity present in accurately modeling all sources of hydrodynamic losses. By applying an irregular wave of $H_s = 2$ m and $\omega_p = 0.5$ rad/s, as shown in Fig. 9(a), R_l is varied from 0% to 100% of the nominal value and the captured energy percentage drop is recorded. Clearly, the R-MPC outperformed the B-MPC, where the maximum energy drop is approximately 5% for R_l increase of 100%, whereas the captured energy is dropped by around 14% under the B-MPC. Similarly, S_b is varied up to 50% of its nominal value. Fig. 9(b) shows that the R-MPC is more robust than the B-MPC, where the maximum energy drop is 24%, versus 35% for the B-MPC.

As mentioned earlier, the hydrodynamic losses force is modeled as a linear force function of the buoy heave velocity, which is used in both

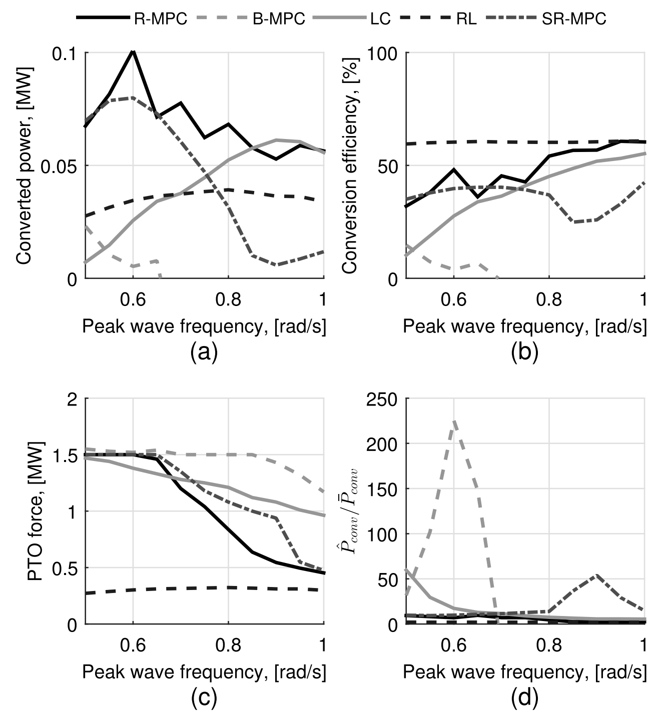

Fig. 7. Performance of the WEC under different control strategies as a function of wave peak frequency (a) average converted power (b) wave-to-wire conversion efficiency (c) maximum PTO force (d) peak-to-average converted power ratio.

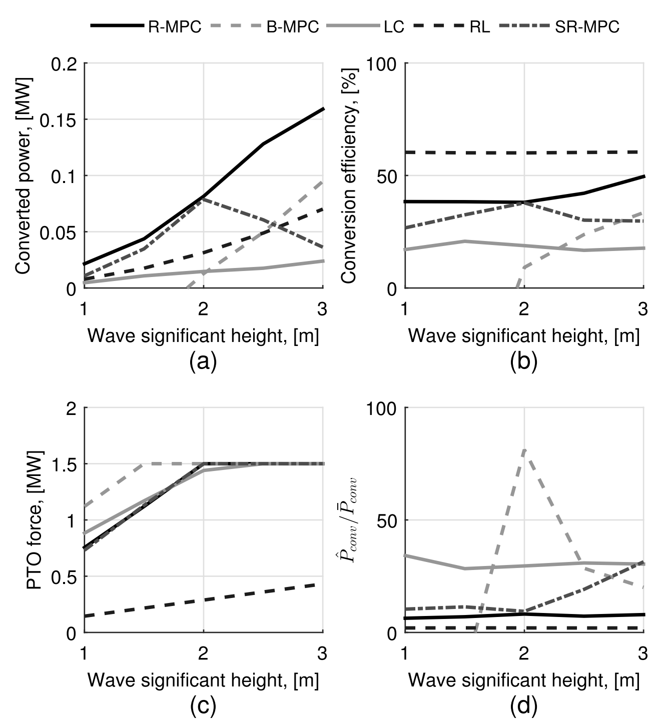

Fig. 8. Performance of the WEC under different control strategies as a function of wave significant height (a) average converted power (b) wave-to-wire conversion efficiency (c) maximum PTO force (d) peak-to-average converted power ratio.

the plant model and in formulating the predictive controllers. Here, the linear term in (3d) is set to zero and the nonlinear viscous drag force is

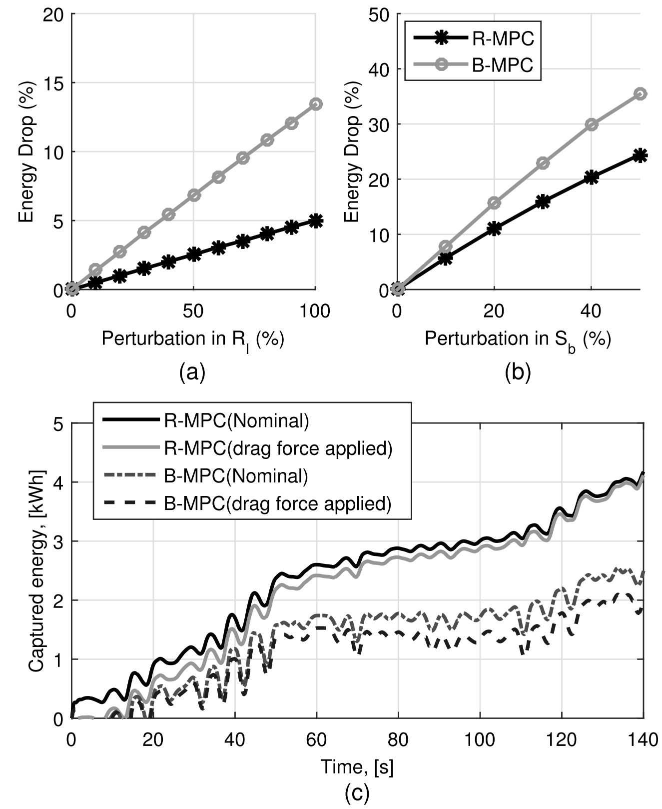

Fig. 9. The performance of the R-MPC and MPC in the presence of (a) structured uncertainty in R_l (b) structured uncertainty in S_b (c) un-modeled nonlinear viscous drag force.

applied on the plant model. This test evaluates how different controllers will react to dynamics which are unknown to them (i.e., not included in their design). As shown in Fig. 9(c), the R-MPC suffered a very slight drop (i.e., 1.6%) in the captured energy after applying the drag force, whereas it dropped by approximately 19% for the B-MPC.

4.4. Sensitivity to disturbances

An aggressive disturbance force $f_{dist}(t)$ is applied in the form of friction force $f_f(t)$ in the PMLG. This might occur as a result of mechanical wear (e.g., bearings damage). Fig. 10(a) describes the friction force which is applied at $t = 40$ s. After applying an irregular wave of $H_s = 2$ m and $\omega_p = 0.5$ rad/s, the R-MPC manages to be less susceptible to $f_{dist}(t)$, where the accumulated captured energy in the presence of $f_{dist}(t)$ is 3.458 kWh, corresponding to 16% drop in the energy compared to the nominal case (4.174 kWh) as shown in Fig. 10(b). On the other hand, the B-MPC resulted in 34% drop in energy.

4.5. Computational performance

In this section, the Laguerre-based MPC is compared with the conventional finite impulse response MPC. The computational performance of both methods were examined. The time it takes to solve a constrained QP problem over a single optimization window of length N_p is computed for both techniques. Note that, for the Laguerre-based MPC, B-MPC is used, that is the local model component is deactivated. The simulations were carried out using a computer that runs a 64-bit Windows 10 operating system, 2.4 GHz Core i7 processor, 16 GB RAM, and MATLAB 2015a. The optimized variable, in this case $f_u(t)$, is plotted for both methods after applying a polychromatic sea-state of $H_s = 2$ m and $\omega_p = 0.5$ rad/s as shown in Fig. 11. It is clear that the Laguerre-based MPC is

Table 2
Computation time (in seconds) needed to solve (18) over single optimization window and at different N_p (in samples) for both conventional and Laguerre-based MPC.

	$N_p = 100$	$N_p = 200$	$N_p = 300$
Laguerre-based MPC	1.41 ms	3.89 ms	10.64 ms
Conventional MPC	3.82 ms	18.28 ms	58.04 ms

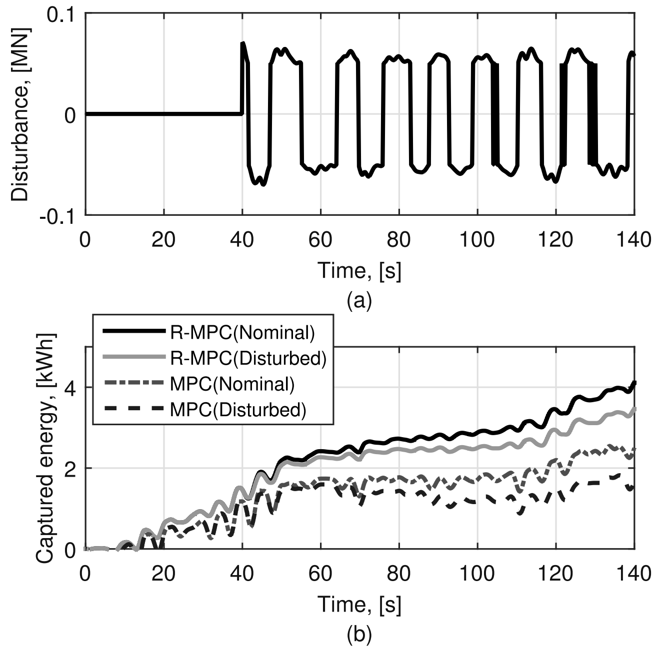

Fig. 10. The performance of the R-MPC and MPC in the presence of external disturbance waveform (a) the PTO friction force waveform (b) captured energy under nominal and disturbed cases for both R-MPC and B-MPC.

in good agreement with the conventional MPC. The discrepancy can be further reduced by increasing the number of Laguerre polynomials N in the Laguerre-based MPC, however, that will be at the expense of the computational speed.

As shown in Table 2, the Laguerre-based MPC proved to be less expensive computationally compared to the conventional MPC. For a prediction horizon N_p of 100 samples (i.e., corresponds to 5 s), Laguerre-based MPC is 2.7 times faster than its counterpart. As N_p increases, the computational superiority of the Laguerre-based MPC increases rather exponentially.

5. Conclusions

In this paper, a robust model predictive control (R-MPC) strategy is proposed to maximize the energy yield of heaving single-body seabed reacting WECs. The computational complexity usually associated with classical MPC has been alleviated by using Laguerre polynomials, which simplifies the real-time deployment of the controller. The simulation results show that the suggested R-MPC strategy outperforms the classical MPC strategy, in which it produces more power at different sea-state characteristics, preserves a unidirectional power flow, and offers a degree of robustness to parametric uncertainties and external disturbances. In addition, the high power conversion efficiency shown by the PMLG indicates that better utilization of the PTO can be achieved under the R-MPC. Computationally, the Laguerre-based MPC outperformed the conventional MPC strategy and the computational superiority even increased as the prediction horizon was increased. To overcome the non-causality associated with estimating the excitation force in real-time realization, short-term prediction methods can be used with the proposed MPC technique.

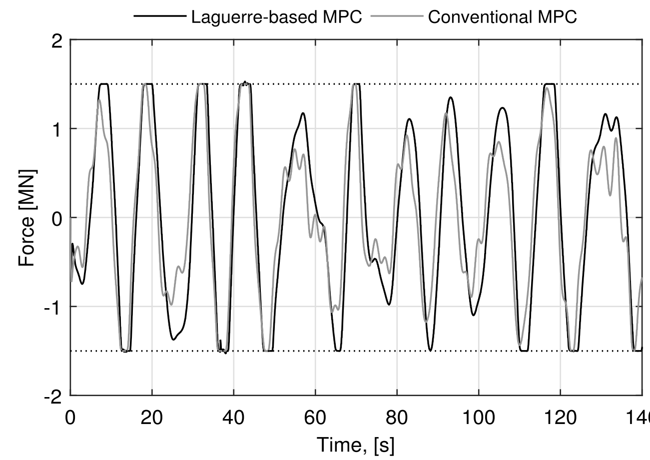

Fig. 11. PTO force $f_u(t)$ profile produced by the proposed Laguerre-based MPC and conventional MPC techniques under a polychromatic sea-state of $H_s = 2$ m and $\omega_p = 0.5$ rad/s.

Acknowledgments

Authors thank UAEU for supporting this research through the UAEU Interdisciplinary Centre-based Program (No. 31R097 and No. 31R103).

Appendix A. Numerical values of the continues state space matrices

The excitation force state matrices:

$$\mathbf{A}_e^{\mathrm{T}} = \begin{bmatrix} -0.7572 & 1 & 0 & 0 & 0 & 0 & 0 & 0 \\ -2.4059 & 0 & 1 & 0 & 0 & 0 & 0 & 0 \\ -1.2517 & 0 & 0 & 1 & 0 & 0 & 0 & 0 \\ -1.7913 & 0 & 0 & 0 & 1 & 0 & 0 & 0 \\ -0.5463 & 0 & 0 & 0 & 0 & 1 & 0 & 0 \\ -0.4217 & 0 & 0 & 0 & 0 & 0 & 1 & 0 \\ -0.0398 & 0 & 0 & 0 & 0 & 0 & 0 & 1 \\ -0.0115 & 0 & 0 & 0 & 0 & 0 & 0 & 0 \end{bmatrix},$$

$$\mathbf{B}_e = \begin{bmatrix} 1 \\ 0 \\ 0 \\ 0 \\ 0 \\ 0 \\ 0 \\ 0 \end{bmatrix}, \mathbf{C}_e^{\mathrm{T}} = \begin{bmatrix} 0.7613 \\ 0.7344 \\ 1.8603 \\ 1.0503 \\ 1.2782 \\ 0.2735 \\ 0.2238 \\ -0.0497 \end{bmatrix}, \mathbf{D}_e = 4.3246 \times 10^5.$$

The radiation force state matrices:

$$\mathbf{A}_r = \begin{bmatrix} -3.4376 & -6.3533 & -4.9714 & -1.7168 \\ 1 & 0 & 0 & 0 \\ 0 & 1 & 0 & 0 \\ 0 & 0 & 1 & 0 \end{bmatrix},$$

$$\mathbf{B}_r = \begin{bmatrix} 1 \\ 0 \\ 0 \\ 0 \end{bmatrix}, \mathbf{C}_r^{\mathrm{T}} = 1 \times 10^5 \begin{bmatrix} 0.9648 \\ 3.6177 \\ 1.5699 \\ 0 \end{bmatrix}.$$

Appendix B. Quadratic programming matrices of the reference velocity generation method

The objective function shown in (35) is made of the following vectors and matrices:

$$\tilde{\mathbf{F}}_{ex,k} = \begin{bmatrix} \tilde{f}_{ex}(k+1|k) \\ \vdots \\ \tilde{f}_{ex}(k+N_w|k) \end{bmatrix}, \mathbf{V}_{r,k} = \begin{bmatrix} v_r(k|k) \\ \vdots \\ v_r(k+N_w-1|k) \end{bmatrix}, \mathbf{R}_l = \begin{bmatrix} R_l \\ \vdots \\ R_l \end{bmatrix},$$

$$\mathbf{Q}_v = \begin{bmatrix} \mathbf{C}_d\mathbf{B}_d & \mathbf{0} & \dots & \mathbf{0} \\ \mathbf{C}_d\mathbf{A}_d\mathbf{B}_d & \mathbf{C}_d\mathbf{B}_d & \ddots & \mathbf{0} \\ \vdots & \ddots & \ddots & \vdots \\ \mathbf{C}_d\mathbf{A}_d^{N_w-1}\mathbf{B}_d & \dots & \mathbf{C}_d\mathbf{A}_d\mathbf{B}_d & \mathbf{C}_d\mathbf{B}_d \end{bmatrix} \in \mathbb{R}^{N_w \times N_w},$$

$$\mathbf{Q}_x = \begin{bmatrix} \mathbf{C}_d\mathbf{A}_d, \mathbf{C}_d\mathbf{A}_d^2, \dots, \mathbf{C}_d\mathbf{A}_d^{N_w} \end{bmatrix} \in \mathbb{R}^{N_w \times 6},$$

$$\mathbf{A}_d = \begin{bmatrix} \mathbf{0}_{2\times2} & \mathbf{0}_{2\times4} \\ \mathbf{0}_{4\times2} & \mathbf{A}_k \end{bmatrix}, \mathbf{B}_d = \begin{bmatrix} 1 \\ 0 \\ \mathbf{B}_k \end{bmatrix}, \mathbf{C}_d = \begin{bmatrix} \mathbf{0}_{1\times2} & \mathbf{C}_k \end{bmatrix}.$$

Note that the state matrices $\mathbf{A}_k, \mathbf{B}_k$, and $\mathbf{C}_k$ are the discrete version of the state matrices in (10). The heave displacement constraint matrices are expressed as follows:

$$\mathbf{Q}_z = \begin{bmatrix} -\mathbf{W}_z & \mathbf{W}_z \end{bmatrix}^T \in \mathbb{R}^{2N_w \times N_w},$$

$$\mathbf{H} = \begin{bmatrix} \mathbf{z}_m + \mathbf{W}_x\mathbf{x}_k & \mathbf{z}_m - \mathbf{W}_x\mathbf{x}_k \end{bmatrix}^T \in \mathbb{R}^{2N_w \times 1},$$

$$\mathbf{z}_m = \begin{bmatrix} z^{max} \dots z^{max} \end{bmatrix}^T \in \mathbb{R}^{N_w \times 1}.$$

The matrices $\mathbf{W}_z$ and $\mathbf{W}_x$ are posed in a similar way as in $\mathbf{Q}_v$ and $\mathbf{Q}_x$, respectively, except that $\mathbf{C}_d$ is modified to $[1\ \mathbf{0}_{1\times5}]$.

Appendix C. Resistive loading and sub-optimal latching control strategies

The PTO force $f_u(t)$ under resistive loading control strategy can be expressed as

$$f_u(t) = -|Z_{in}(\omega_p)|v(t),$$

where

$$|Z_{in}(\omega_p)| = \sqrt{R_r(\omega_p)^2 + \left(\omega_p(m_b + M_r(\omega_p)) - (S_b + S_{rs})/\omega_p\right)^2}$$

where $R_r(\omega_p)$ and $M_r(\omega_p)$ are the radiation resistance and added mass, respectively. The PTO force $f_u(t)$ under the sub-optimal latching control can be represented as follows:

Algorithm 1 Sub-optimal latching control algorithm

Input: $f_{ex}(t)$ and $v(t)$
Output: $f_u(t)$
if Buoy velocity $v(t)$ becomes zero **or** both $f_{ex}(t)$ and $v(t)$ are not in the same direction **then**
  The buoy is LATCHED and $f_u(t) = f_t(t)$
else if The buoy is already LATCHED **and** the wave excitation force $f_{ex}(t)$ changes direction (sign) **then**
  The buoy is UN-LATCHED and $f_u(t) = 0$
end if

When the buoy is latched, the PTO force $f_u(t)$ is equal to the total force $f_t(t)$, which in turn is equal to the summation of $f_h(t)$, $f_{rs}(t)$, $f_f(t)$, and $|Z_{in}(\omega_p)|v(t)$. The last term represents a resistive loading (damping) force required to assist in the latching process.

References

Bacelli, G., & Ringwood, J. (2015). Numerical optimal control of wave energy converters. *IEEE Transactions on Sustainable Energy*, *6*, 294–302.

Ballard, Z., & Mann, B. (2013). Two-dimensional nonlinear analysis of an untethered spherical buoy due to wave loading. *Journal of Computational and Nonlinear Dynamics*, *8*, 041019(1)–041019(12).

Boldea, I., & Nasar, S. (1997). *Linear electric actuators and generators*. Cambridge, UK: Cambridge University Press.

Brekken, T. (2011). On model predictive control for a point absorber wave energy converter. In *IEEE Trondheim PowerTech* (pp. 1–8).

Budal, K., & Falnes, J. (1980). *Interacting point absorber with controlled motion, in the power from sea waves*. BM Count: Academic Press.

Eriksson, M. (2007). *Modelling and experimental verification of direct drive waveenergy conversion* (Ph.D. thesis), Uppsala University.

Falnes, J. (2002). *Ocean waves and oscillating systems*. Cambridge University Press.

Feng, W., Zhang, X., Ju, P., & Sterling, M. (2008). Modeling and control of AWS-based wave energy conversion system integrated into the power grid. *IEEE Transactions on Power Systems*, *23*, 1196–1204.

Fliess, M., & Join, C. (2008). Non-linear estimation is easy. *International Journal of Modelling Identification and Control*, *1*, 12–27.

Fliess, M., & Join, C. (2013). Model-free control. *International Journal of Control*, *86*, 2228–2252.

Fusco, F., & Ringwood, J. (2010). Short-term wave forecasting for real-time control of wave energy converters. *IEEE Transactions on Sustainable Energy*, *1*, 99–106.

Fusco, F., & Ringwood, J. (2014a). Hierarchical robust control of oscillating wave energy converters with uncertain dynamics. *IEEE Transactions on Sustainable Energy*, *5*, 958–966.

Fusco, F., & Ringwood, J. (2014b). A simple and effective real-time controller for wave energy converters. *IEEE Transactions on Sustainable Energy*, *4*, 21–30.

Guo, B., Patton, R., Jin, S., & Lan, J. (2018). Numerical and experimental studies of excitation force approximation for wave energy conversion. *Renewable Energy*, *125*, 877–889.

Hals, J., Falnes, J., & Moan, T. (2011). Constrained optimal control of a heaving buoy wave-energy converter. *Journal of Offshore Mechanics and Arctic Engineering*, *133*, 011401.

Jaen, A., Andrade, D., & Santana, A. (2013). Increasing the efficiency of the passive loading strategy for wave energy conversion. *Journal of Renewable and Sustainable Energy*, *5*, 053132.

Jama, M. (2015). *Control strategies for improving the performance of heaving wave energy converters* (Ph.D. thesis), UAE University.

Jama, M., Noura, H., Wahyudie, A., & Assi, A. (2015). Enhancing the performance of heaving wave energy converters using model-free control approach. *Renewable Energy*, *83*, 931–941.

Jama, M., Wahyudie, A., Assi, A., & Noura, H. (2013). Controlling heaving wave energy converter using function-based model predictive control technique. In *2013 25th Chinese control and decision conference, CCDC* (pp. 2705–2710).

Jama, M., Wahyudie, A., Assi, A., & Noura, H. (2014). Function-based model predictive control aproach for maximum power capture of heaving wave energy converters. In M. Hamdan, H. Hejazy, H. Noura, & A. Fardoun (Eds.), *Renewable energy: Generation and applications*. ICREGA'14, (pp. 299–313). Switzerland: Springer International Publishing.

Krantz, S. (2002). *The implicit function theorem*. Boston: Birkhauser.

Li, G. (2015). Predictive control of a wave energy converter with wave prediction using differential flatness. In *Proceedings of IEEE 54th annual conference n decision and control, CDC*.

Li, G., & Belmont, M. (2014). Model predictive control of sea wave energy converters — Part I: A convex aproach for the case of a single device. *Renewable Energy*, *69*, 453–463.

McCormick, M. (2010). *Ocean engineering mechanics with applications*. Cambridge, UK: Cambridge University Press.

Reger, J., Ramirez, H., & Fliess, M. (2005). On non-asymptotic observation of nonlinear systems. In *Proc 44th IEEE conf on decision and control, CDC*.

Richter, M., Magana, M., Sawodny, O., & Brekken, T. (2013). Nonlinear model predictive control of a point absorber wave energy converter. *IEEE Transactions on Sustainable Energy*, *4*, 118–126.

Sheng, W., Alcorn, R., & Lewis, A. (2015). On improving wave energy conversion, part II: Development of latching control technologies. *Renewable Energy*, *75*, 935–944.

Sul, S. K. (2011). *Control of electric machine drive systems*. New Jersey, USA: Wiley Sons.

Taghipoura, R., Pereza, T., & Moan, T. (2008). Hybrid frequency-time domain models for dynamic response analysis of marine structures. *Ocean Engineering*, *35*, 685–705.

Tedeschi, E., & Molinas, M. (2012). Tunable control strategy for wave energy converters with limited power takeoff rating. *IEEE Transactions on Industrial Electronics*, *59*, 3838–3846.

Timmerman, P., & Weelea, J. (1999). On the rise and fall of a ball with linear or quadratic drag. *American Journal of Physics*, *68*, 538–546.

Wahyudie, A., Jama, M., Saeed, O., Nandar, C., & Harib, K. (2015). Robust and low computational cost controller for improving captured power in heaving wave energy conveters. *Renewable Energy*, *82*, 114–124.

Wahyudie, A., Jama, M., Saeed, O., Nandar, C., & Harib, K. (2017). Simpole bottom-up hierarchical control strategy for heaving wave energy converters. *International Journal of Electrical Power and Energy*, *87*, 211–221.

WAMIT, (2006). *User manual*. WAMIT, Inc., (Accessed 24 June 2016). www.wamit.com.

Wang, L. (2001). Continuous time model predictive control using orthonormal functions. *International Journal of Control*, *74*, 1588–1600.

Wang, L. (2009). *Model predictive control system design and implementation using MATLAB*. Spring.

Wang, X., Sun, X., Li, S., & Ye, H. (2001). Output feedback domination approach for finite-time force control of an electrohydraulic actuator. *IET Control Theory & Applications*, *6*, 921–934.

Xi, Y., Li, D., & Lin, S. (2013). Model predictive control-state and challenges. *Acta Automatica Sinica*, *39*, 222–236.

Yang, X. (2010). *Engineering optimization: An introduction with metaheuristic applications*. Wiley & Sons.

Yousef, A. M., & Kassem, A. M. (2012). Stand alone wind energy conversion system based on functional predictive control. *International Journal of Green Energy*.